Probing the Mutation Independent Interaction of DNA Probes with

SARS-CoV-2 Variants Through a Combination of Surface-Enhanced

Raman Scattering and Machine Learning

Parikshit Moitra, a Ardalan Chaichi, e Syed Mohammad Abid Hasan, e Ketan Dighe, a,d

Alisha Prasad, e Maha Alafeef, a,c,d,f Manas Ranjan Gartia, e and Dipanian Pan*,a,b,c,d

^a Department of Pediatrics, Center for Blood Oxygen Transport and Hemostasis,

University of Maryland Baltimore School of Medicine, Baltimore, Maryland 21201, United

States

^b Department of Diagnostic Radiology and Nuclear Medicine, University of Maryland

Baltimore School of Medicine, Baltimore, Maryland 21201, United States

^c Bioengineering Department, University of Illinois at Urbana-Champaign, Urbana, Illinois

61801, United States

^d Department of Chemical, Biochemical, and Environmental Engineering, University of

Maryland Baltimore County, Baltimore, Maryland 21250, United States

e Department of Mechanical and Industrial Engineering, Louisiana State University, Baton

Rouge, Louisiana 70803, United States

f Biomedical Engineering Department, Jordan University of Science and Technology, Irbid

22110, Jordan.

Corresponding Author

*Prof. Dipanjan Pan, Email: dipanjan@som.umaryland.edu

*Dr. Manas Gartia, Email: mgartia@lsu.edu

Keywords. SARS-CoV-2 variants; mutation resistant probe; antisense oligonucleotide; surface-enhanced Raman scattering; selective and ultrasensitive diagnosis.

Abstract.

Severe acute respiratory syndrome coronavirus 2 (SARS-CoV-2) evolution has been characterized by the emergence of sets of mutations impacting the virus characteristics, such as transmissibility and antigenicity, presumably in response to the changing immune profile of the human population. The presence of mutations in the SARS-CoV-2 virus can potentially impact therapeutic and diagnostic test performances. We design and develop here a unique set of DNA probes i.e., antisense oligonucleotides (ASOs) which can interact with genetic sequences of the virus irrespective of its ongoing mutations. The probes, developed herein, target a specific segment of the nucleocapsid phosphoprotein (N) gene of SARS-CoV-2 with high binding efficiency which do not mutate among the known variants. Further probing into the interaction profile of the ASOs reveals that the ASO-RNA hybridization remains unaltered even for a hypothetical single point mutation at the target RNA site and diminished only in case of the hypothetical double or triple point mutations. The mechanism of interaction among the ASOs and SARS-CoV-2 RNA is then explored with a combination of surface-enhanced Raman scattering (SERS) and machine learning techniques. It has been observed that the technique, described herein, could efficiently discriminate between clinically positive and negative samples with ~100%

sensitivity and ~90% specificity up to 63 copies/mL of SARS-CoV-2 RNA concentration. Thus, this study establishes N gene targeted ASOs as the fundamental machinery to efficiently detect all the current SARS-CoV-2 variants regardless of their mutations.

1. Introduction.

The decline in coronavirus disease – 2019 (COVID-19) cases in much of the world in late spring and early summer signaled a new phase in the fight against the disease (Telenti et al., 2021). This progress was made possible by the rapid deployment of vaccines (Mallapaty et al., 2021). However, due to emerging new variants such as Beta, Delta, Lambda, and most recently Omicron, as well as the vaccine reluctance, nations across the globe have witnessed an alarming increase in COVID-19 cases in recent months (Callaway and Ledford, 2021; Karim and Karim, 2021). As a result, it continues to spread rapidly throughout the world, causing unprecedented disruption in modern society. While vaccines continue to be extremely effective at preventing serious illness caused by COVID-19, new data from the United Kingdom (U.K.), Israel, and the U.S. have raised new concerns about their ability to prevent infection from the delta as well as more transmissible and potentially concerning Omicron variant (Janik et al., 2021; Mercatelli and Giorgi, 2020; L. Wang et al., 2021). Furthermore, while the Omicron variant fuels a fresh wave of infections, decline in extensive testing and monitoring together with the unavailability of an effective diagnostic test to selectively detect these emerging variants without any false negativity, makes it impossible to determine how much the virus is circulating in communities and who remains most vulnerable (Daria et al., 2021; Mohiuddin and Kasahara, 2022).

These SARS-CoV-2 genetic variants represent permanent changes in the DNA sequence and may affect three or more nucleotides in a gene (Pachetti et al., 2020). These alterations may result into failure of diagnostics, reduction in vaccine effectiveness, low vaccine-induced protection against severe disease, more severe clinical disease, and significantly diminished susceptibility to diagnostics or approved therapeutics (Barton et al., 2021; Dighe et al., 2021; Liu et al., 2021; P. Wang et al., 2021). As new variants continue to emerge, a deeper understanding of the phenotypes of these variants in terms of infectivity, transmissibility, virulence, and antigenicity must be gained (Copin et al., 2021; Liu et al., 2021). As a result, there is still an unmet requirement for routine largescale comprehensive testing to prevent COVID-19 spread and provide safe environments for socio-economic activities. And we believe that this can only be done by developing a probe that will interact with all the variants of SARS-CoV-2 independent of their mutations. Unpredicted combinations of mutations will continue to emerge, such perceptions will allow predictions of virus phenotype (Jungreis et al., 2021; Petrova and Russell, 2018) and in turn, help to develop newer probes for mutation independent interaction with SARS-CoV-2 genes.

In this regard, here we have designed and developed several sets of novel DNA Probes, i.e., antisense oligonucleotides, targeted towards nucleocapsid phosphoprotein (N), envelope (E) and RNA-dependent RNA polymerase (RdRp) gene segments of SARS-CoV-2. We hypothesized that a combination of computational and vibrational spectroscopic techniques along with machine learning (ML) algorithm can be applied to study the mutation-independent interaction of these DNA probes with SARS-CoV-2 RNA. Following the successful design and synthesis, these ASOs were connected to gold

nanoparticles (AuNPs) and their target binding energies and agglomeration patterns were then investigated in presence of SARS-CoV-2 RNA. We found that N-gene targeted ASOs were the most efficient ones in selectively hybridizing SARS-CoV-2 target RNA with optimum efficiency. The target RNA sites for N-gene ASOs were then examined against the current SARS-CoV-2 variants where it was found that these ASOs should interact with all the known mutated forms of SARS-CoV-2 in a similar manner without any loss in sensitivity and specificity. The mechanism of interaction between these N genetargeted ASOs and SARS-CoV-2 RNA was then evaluated with surface-enhanced Raman scattering (SERS) and machine learning (ML) techniques (Abid Hasan et al., 2019; Chaichi et al., 2021; Chang et al., 2015; Gartia et al., 2010; Prasad et al., 2020; Xu et al., 2012, 2011). This combinatorial effort discriminated SARS-CoV-2 positive and negative clinical nasal swab samples with ~100% sensitivity and ~90% specificity with an analytical detection limit of 63 copies/mL. However, the characterization of different SARS-CoV-2 N-gene mutated forms will continue to evolve and provide extremely useful information on specific mutations or their combinations those may not have been identified yet in circulating viruses (Harvey et al., 2021). Towards this goal, we computationally evaluated next hypothetical single, double, and triple point mutations on the RNA site. Further close monitoring of the ASO-RNA hybridization profile revealed stable interaction between the two, even after a hypothetical single point mutation was introduced at the target RNA site. Thus, this study examined the efficiency of universal DNA probes and their fundamental interaction with the entire known mutated forms of SARS-CoV-2.

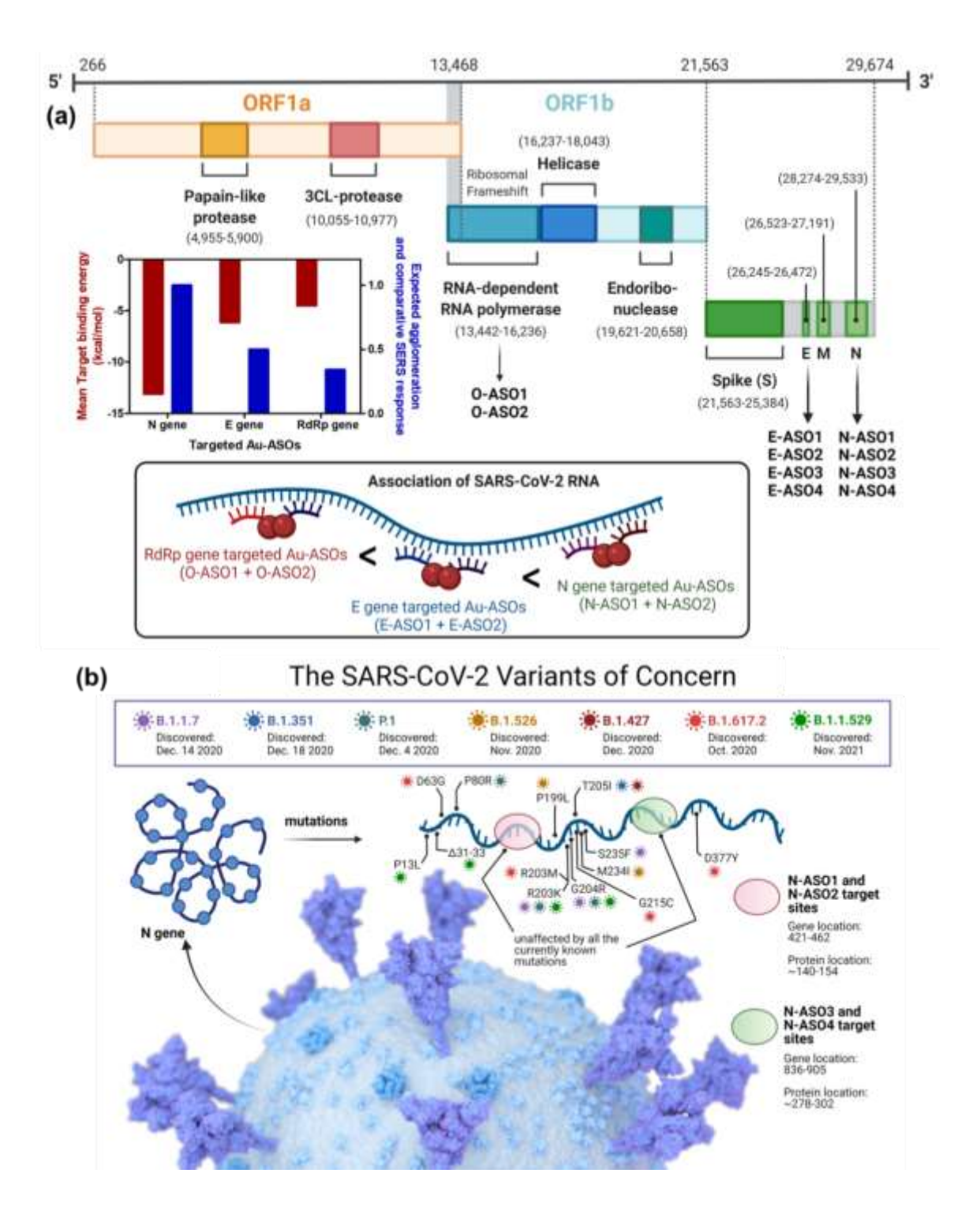


Fig. 1. (a) Genomic organization of SARS-CoV-2 and its schematic agglomeration pattern with gold nanoparticles differentially functionalized with antisense oligonucleotides

targeted towards different genetic segments; (b) Currently known N gene mutation sites for SARS-CoV-2 and their alignment with the targeted sites of the developed ASOs.

2. Results and Discussion.

We designed and developed novel ASOs targeted towards different genetic segments of SARS-CoV-2, *e.g.*, N, E and RdRp gene for the selective and sensitive binding of RNA from the wild type of SARS-CoV-2. More importantly, herein, we investigated the mechanism of interaction of selected ASOs with the various mutated forms of SARS-CoV-2 and studied the ASO-RNA hybridization phenomena through a unique combination of SERS and ML-based techniques.

2.1. Design of SARS-CoV-2 targeted ASOs. Accordingly, particular gene sequences (RdRp: 13,442-16,236; E: 26,245-26,472 and N: 28,274-29,533) from the whole genome sequence of SARS-CoV-2 (wild type isolate SARS-CoV-2/human/USA/WA-CDC-WA1-A12/2020, MT020880) was chosen and multiple ASO sequences of 20 nucleotides in length were developed (Fig. 1a). The choice of ASOs were primarily based on the optimum GC content and theoretically calculated target binding and disruption energies at 37 °C in 1 M NaCl aqueous solution. We propose to select four ASOs, two for the front (ASO1 and ASO2), and two targeting the end region (ASO3 and ASO4) of the gene. The ASOs will also target closely following sequences at each location (Alafeef et al., 2021a, 2021b, 2020; Dighe et al., 2021; Moitra et al., 2021b, 2021a, 2020). Accordingly, four ASOs were selected both for N and E genes, whereas only two were selected for the RdRp gene as ASOs with high enough binding energies are not available for this target

(Table 1). Soligo software were used to predict the ASOs (Ding et al., 2004). The detailed methodology is discussed in the method section of supporting information. It was noticed that the mean target binding energy was the highest for N gene-targeted ASOs (N-ASO1-4) and decreased gradually for E gene-targeted ASOs (E-ASO1-4) and was the minimum for RdRp targeted ones (O-ASO1-2). Based on this theoretical observation, it can also be presumed that the effective ASO-RNA hybridization will follow the same trend and will be the highest for N-ASO1 and N-ASO2. We anticipated that once these ASOs were connected to a plasmonic nanoparticle, such as AuNPs, the agglomeration among ASO capped AuNPs would exhibit a strong SERS response (Khan et al., 2018; Misra et al., 2018; Moitra et al., 2020; Pan et al., 2011, 2010) and should also exhibit similar phenomena where a mixture of N-ASO1 and N-ASO2 may be the optimum one (Fig. 1a).

Table 1. Sequences of the differentially functionalized antisense oligonucleotides targeted towards different segments of SARS-CoV-2 isolate 2019-nCoV/USA-WA1-A12/2020 (MT020880). The targeted segments are N gene (28274..29533), E gene (26245..26472) and part of the RDRP gene (13442..16236: a part of the ORF1ab).

					Bindin	Target
Target	Target	sequence	ASO sequence (5p—	GC	g site	bindin
position	(5p—3p)		3p)	cont	disrupt	g
				ent	ion	energy
					energy	oe.gy

				(kcal/ mol)	(kcal/ mol)
Target ge	ne N				
28694- 28713	ACACCAAAAGAUC ACAUUGG	HS-C6- CCAATGTGATCTTTT GGTGT (N-ASO1)	40%	7.6	-15.8
28716- 28735	CCCGCAAUCCUG	ATTGTTAGCAGGATT GCGGG-C6-SH (N- ASO2)	50%	7.6	-10.4
29109- 29128	CAGAACAAACCCA AGGAAAU	HS-C6- ATTTCCTTGGGTTTG TTCTG (N-ASO3)	40%	6.0	-14.3
29159- 29178	ACUGAUUACAAAC AUUGGCC	GGCCAATGTTTGTAA TCAGT-C6-SH (N- ASO4)	40%	8.7	-10.0
Target ge	ne E				

26306- 26325	UUGCUUUCGUGG UAUUCUUG	HS-C6- CAAGAATACCACGAA AGCAA (E-ASO1)	40%	12.4	-5.5
26331- 26350	UACACUAGCCAUC CUUACUG	CAGTAAGGATGGCT AGTGTA-C6-SH (E-ASO2)	45%	15.0	-6.7
26366- 26385	CGUACUGCUGCA AUAUUGUU	HS-C6- AACAATATTGCAGCA GTACG (E-ASO3)	40%	4.9	-8.8
26390- 26409	UGAGUCUUGUAA AACCUUCU	AGAAGGTTTTACAAG ACTCA-C6-SH (E-ASO4)	35%		-4.3
Target gene RdRp of ORF1b					
15361- 15380	AAACAUACAACGU GUUGUAG	HS-C6- CTACAACACGTTGTA TGTTT (O-ASO1)	35%		-6.4
15389- 15408	ACCGUUUCUAUA GAUUAGCU	AGCTAATCTATAGAA ACGGT-C6-SH (O-ASO2)	35%		-2.6

2.2. Selective hybridization of ASOs with SARS-CoV-2 RNA. To prove this theoretical assumption, we differentially modified the ASOs, one at the 5' end and the other at the 3' end by thiol groups (Table 1). The thiol modified ASOs were then used to cap the citrate stabilized AuNP (Moitra et al., 2020; Zhu et al., 2021). The agglomeration patterns of these ASOs conjugated to AuNPs (Au-ASO NPs) were then investigated in presence of RNA extracted from clinically positive and negative SARS-CoV-2 samples. We employed UV-Visible absorbance spectroscopy and dynamic light scattering (DLS) to initially investigate the aggregation phenomena. SARS-CoV-2 positive nasal swab samples (N=10) having varying cycle threshold (Ct) numbers from 13 to 28 (Table S1) were considered and RNA was extracted from these samples by standard protocol (Rump et al., 2010; Wozniak et al., 2020). Representative two samples, one having low Ct number (P1), i.e., high viral copy number and the other having high Ct value (P2), i.e., low viral copy number, was considered for this study. It was observed that the absorbance of plasmonic Au-ASO NPs at 520 nm increased with broadening of full-width half maximum (FWHM) when added with SARS-CoV-2 positive RNA. P1 having a high viral copy number increased the absorbance more than P2 which had a low viral copy number. An insignificant increase in absorbance with no change in FWHM was observed when Au-ASO NPs were added with SARS-CoV-2 negative RNAs. This change in surface plasmon band of AuNPs indicated the successful aggregation of Au-ASO NPs only in presence of their target RNAs. (Moitra et al., 2020; Ostadhossein et al., 2020; Rump et al., 2010; Srivastava et al., 2020) It was also observed that the mixture of N-ASO1 and N-ASO2 gave a better aggregation response than the mixture having N-ASO3 and N-ASO4 (Fig. 2a). Similar is the case for E-ASO1 and E-ASO2 compared to the combination of E-ASO3

and E-ASO4 (**Fig. 2b**). Further, the change in absorbance was found to be the highest for N-ASO1 and N-ASO2, followed by E-ASO1 and E-ASO2 and the minimum for O-ASO1 and O-ASO2 (**Fig. S1**). This improved agglomeration of N-ASO1 and N-ASO2 mixture in presence of SARS-CoV-2 RNA was further supported by DLS experiments. The average hydrodynamic diameter was found to be the highest for N-ASO1 and N-ASO2 mixture in presence of RNA extracted from P1 compared to the other mixture of Au-ASO NPs (**Fig. 2d**). Thus, these experiments corroborated with our theoretical observation supporting better binding followed by improved ASO-RNA hybridization in case of N-ASO1 and N-ASO2 mixture.

2.3. Mutation independent interaction of SARS-CoV-2 RNA with N-gene targeted ASOs. This interesting observation, where we found that N-gene targeted ASOs were more efficient than E gene and RdRp gene-targeted ASOs in hybridizing SARS-CoV-2 RNA, led to the curiosity to investigate these N-ASOs more closely. We asked the question whether these ASOs will still be effective against the current SARS-CoV-2 mutations or not. We realized that the viability of the assay can be improved significantly if a mostly conserved region of N-gene sequence can be targeted by the ASO probes. Accordingly, the design of N-ASOs was revisited and the target RNA sites for these ASOs were examined against the current SARS-CoV-2 variants. Recently, the genetic surveillance of SARS-CoV-2 strains circulating around the world has revealed several variants with one or more mutations that may affect detection by nucleic acid-based testing methods (Carter et al., 2020; Yu et al., 2021).

It was observed that the currently known mutations associated with SARS-CoV-2 variants mostly occur at 606-617, 702-704 and 1131-1133 of N-gene sequence (**Table**

S2) (Gitman et al., 2021; Kevadiya et al., 2021; Li et al., 2021). Fig. 1b summarizes known SARS-CoV-2 variants and the impact, if any, on the developed assay based on bioinformatic analysis. It was observed that our DNA probes uniquely targets regions of the N gene (ASO1 starting 421 and ending with 440; ASO2 from 443 to 462; ASO3 from 836 to 855 and ASO4 from 886 to 905) which is unaffected by all the currently known N-gene mutations associated with SARS-CoV-2 variants including Omicron, the most mutated form of SARS-CoV-2. We are, therefore, confident that our ASO-based probes will bind to the RNA of SARS-CoV-2 of any variant without any false-negative signals. In addition to this, the mutations in other regions of the genome, such as in the spike protein, membrane or envelope protein, have no impact on the binding of these probes with the SARS-CoV-2 RNA. Therefore, the reliability and reproducibility of the current probes increase based on its design of simultaneous targeting of two of the N-gene regions of SARS-CoV-2, ensuring the feasibility of using these probes even if one region of the viral gene undergoes mutation during its current spread (Fig. 1).

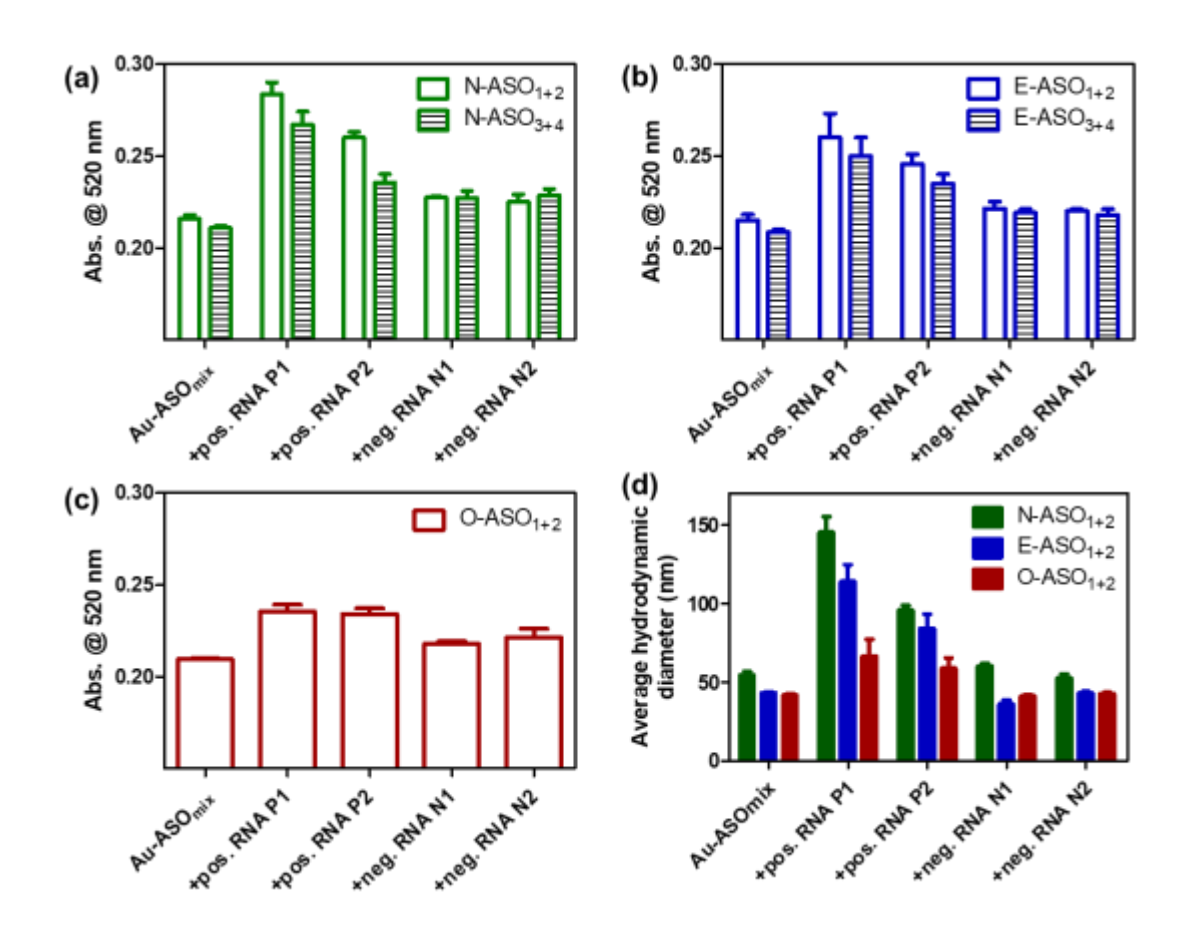


Fig. 2. Aggregation induced change in absorbance at 520 nm for the differentially functionalized Au-ASO NPs targeted for (a) N gene; (b) E gene and (c) RdRp gene upon the addition of RNAs (1 μL) extracted from clinically positive and negative SARS-CoV-2 samples. (d) Comparative change in average hydrodynamic diameter among the different Au-ASO NPs upon the addition of RNAs. In each case, the mixture was incubated for 15 min at room temperature prior to recording the change in absorbance. Ct value of positive RNA P1 and P2 are 14.7 and 27 respectively by RT-PCR analyses which correspond to 107186 and 781 copies/μL of SARS-CoV-2 RNA.

2.4. Probing the mechanism of ASO-RNA hybridization by surface-enhanced **Raman spectroscopy.** It was understood that the prime reason behind this extraordinary specificity of the probes irrespective of the known SARS-CoV-2 mutations was the befitting interaction of the N-ASOs with their target SARS-CoV-2 RNA samples. We, therefore, became interested to study the fundamental basis of interaction of these N gene-targeted Au-ASO NPs (N-ASO₁₊₂ AuNPs) and SARS-CoV-2 RNA by Raman scattering utilizing the intrinsic surface plasmon resonance of Au-ASO NPs as Raman reporters (Abid Hasan et al., 2019; Chang et al., 2015; Xu et al., 2012). It was envisaged that N-ASO₁₊₂ AuNPs, when targeting particular regions in the gene locations of SARS-CoV-2, will start to agglomerate because of their proximity in the gene sequences (Alafeef et al., 2020; Moitra et al., 2020). This will cause a change in surface plasmon resonance and introduce a change in the SERS response of the AuNPs (Gitman et al., 2021; Kevadiya et al., 2021; Shrivastav et al., 2021). The N-ASO₁₊₂ capped AuNPs were synthesized and analytically characterized by UV-Visible spectroscopy (Fig. S2) and transmission electron microscopy (Fig. S3). The nanoparticles were then admixed with SARS-CoV-2 RNA and the corresponding bright field and Raman microscopic images for N-ASO₁₊₂ capped AuNPs are shown in **Fig. 3a**, **b**. The representative Raman spectra of N-ASO₁₊₂ capped AuNPs at varying concentrations of SARS-CoV-2 RNA ranging from 624.4 copies/mL to 2.5×10^{11} copies/mL are shown in **Fig. 3c** where the SERS response of the nanoparticles increased with increase in RNA concentration. This confirmed the enhanced agglomeration among the N-ASO₁₊₂ capped AuNPs in presence of increasing concentration of SARS-CoV-2 RNA. It was observed that the Raman peaks specific for oligonucleotide backbone, ribose and deoxyribose sugars were visible both at low viral

RNA concentration, i.e., 63 copies/mL (**Fig. 3d**), and at high viral RNA concentration, i.e., 6.3 × 10⁷ copies/mL (**Fig. 3e**) indicating efficient hybridization among the ASOs and their target RNA strands (Abid Hasan et al., 2019; Gartia et al., 2010). Raman peaks were accordingly assigned for both concentrations and enlisted in **Table S3 and S4**. The limit of detection for N-ASO₁₊₂ capped AuNPs towards SARS-CoV-2 RNA was also evaluated and found to be 63 copies/mL which is quite significant and highly comparable to the currently available RT-PCR techniques (**Fig. 3f**).

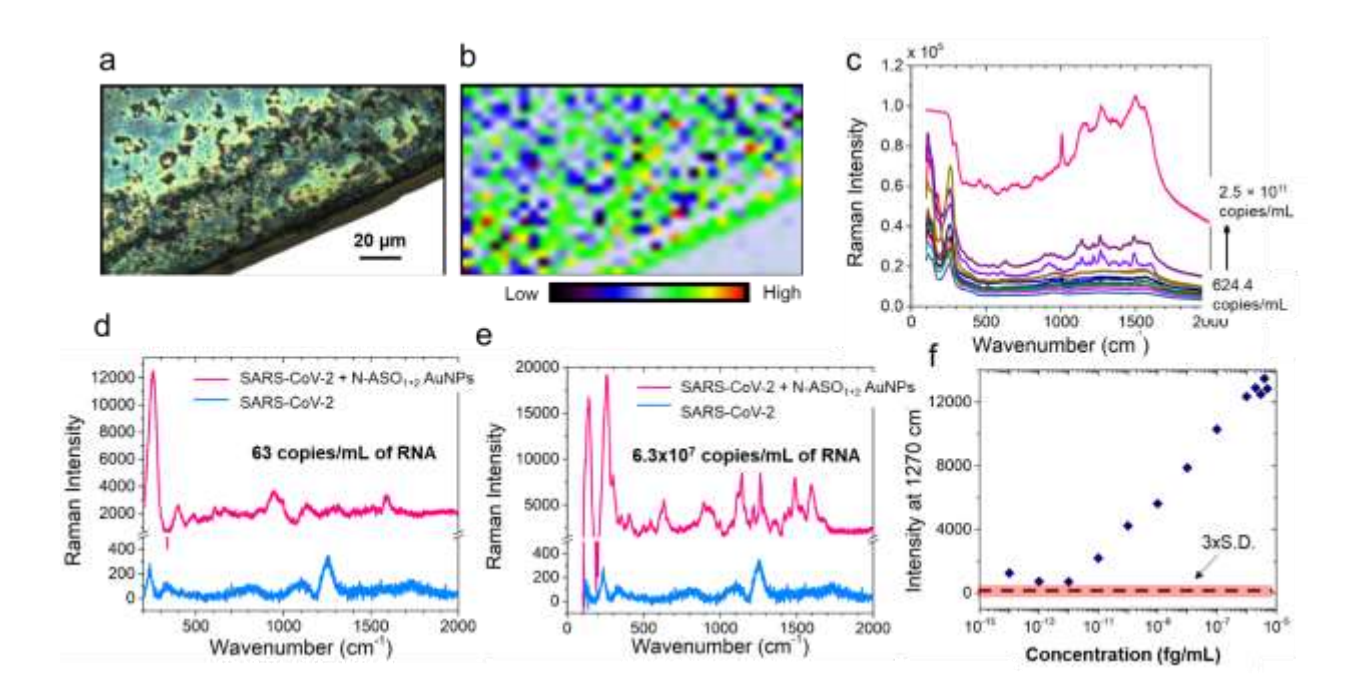


Fig. 3. (a) Bright field image of N-ASO₁₊₂ capped AuNPs admixed with SARS-CoV-2 RNA; (b) Raman microscopic image of SARS-CoV-2 RNA associated N-ASO₁₊₂ capped AuNPs in the range of 1495-1602 cm⁻¹ (785 nm laser, 100% power, grating of 1200, 50 XL magnification) with the center of 1200 cm⁻¹. Red means higher concentration and blue indicates lower concentration of sample; (c) Raman spectra of N-ASO₁₊₂ capped AuNPs at varying concentrations of SARS-CoV-2 RNA ranging from 624.4 copies/mL to 2.5 × 10¹¹ copies/mL; (d, e) Raman spectra of N-ASO₁₊₂ capped AuNPs mixed with SARS-

CoV-2 RNA at low (63 copies/mL) and high concentration (6.3 × 10⁷ copies/mL) respectively; (f) Limit of detection of N-ASO₁₊₂ capped AuNPs towards the detection of SARS-CoV-2 RNA. Here, 1 fg/mL corresponds to 63 copies/mL of SARS-CoV-2 RNA.

2.5. Studying the interaction of direct clinical samples with N-ASO capped AuNPs.

The high sensitivity of N-ASO₁₊₂ capped AuNPs towards the binding of SARS-CoV-2 RNA grew our confidence to study the interaction in clinical nasal swab samples either as COVID-19 positive or negative. We presumed that because of this strong and efficient hybridization among the ASOs and RNA, the binding interaction might be evident even from the direct clinical samples without the extraction and purification of SARS-CoV-2 RNA (Alafeef et al., 2021b; Dighe et al., 2021). Accordingly, samples were treated with lysis buffer containing guanidine isothiocyanate and mixed with N-ASO₁₊₂ capped AuNPs to record their Raman spectra. While for the nanoparticles mixed with SARS-CoV-2 RNA 1500 individual Raman spectra were acquired, for direct clinical samples, 2500 Raman spectra were acquired for each of the samples. The respective Raman spectra for N-ASO₁₊₂ capped AuNPs added with RNA extracted from SARS-CoV-2 positive, P1 (Fig. 4a) and negative, N1 (Fig. 4b) clinical samples were shown. The respective Raman spectra of N-ASO₁₊₂ capped AuNPs admixed with direct SARS-CoV-2 positive (Fig. 4d) and negative (Fig. 4e) clinical samples were also shown without the extraction of RNA but with just the addition of lysis buffer. The range of all the acquired spectra are shown as shaded color for each sample while the dark color is representing the mean spectra for each of the sample. The Raman peaks were assigned for the spectra in Fig. 4a, 4b and enlisted in Table S5. Raman peaks were also assigned for Fig. 4d, 4e and noted in

Table S6. Based on this dataset, we performed the principal component analysis (PCA) and PCA score plot showing the separation between negative and positive RNA samples (Fig. 4c) and direct clinical samples (Fig. 4f). From these figures, it can be noticed that due to possible interference from sample matrix (background signal), PCA was not able to accurately distinguish negative samples from the positive ones. Though, there were some clusters of points on two sides, but a good amount of overlap was also present. Here, each point is representing the Raman spectra of each sample. However, we calculated several numbers of principal components (PCs) for these analyses where we found that PC1 shifted to negative values for SARS-CoV-2 positive RNA samples. On the other hand, PC3shifted to positive values for SARS-CoV-2 positive clinical samples (Fig. 4c, f). Fig. S4 shows the contribution PCs for clinical samples. Here, we compared the Eigenvalues calculated from PCA with respect to principal components number. It can be seen that the first five principal components described more than 99% of the variation of the corresponding dataset. Fig. S5 and S6 show the loading plots for PCA of clinical samples for PC3 and PC1 respectively. Here, we highlighted the characteristic peaks of our dataset which indicated the differences in the various samples. It was noticeable that in both of these figures the location of the characteristic peaks was very similar. This indicated the variation of all the datasets was not significant enough and thus it led to the overlap in the score plot as observed in Fig. 4c, 4f. Fig. S7 shows the box plot for the distribution of spectral data for positive and negative groups of clinical samples. The spectral data of the negative samples from the dataset significantly (P < 0.001) shifted towards the negative PC 3 range compared to positive samples. Although, PC1 and PC3 could be used to distinguish positive and negative RNA as well as clinical samples,

respectively, we further explored the diagnostic capability of these binary classification (positive vs negative) systems. The score plot shown in Figure 4c and 4f pointed to a less accurate classification system using the PCA scores alone.

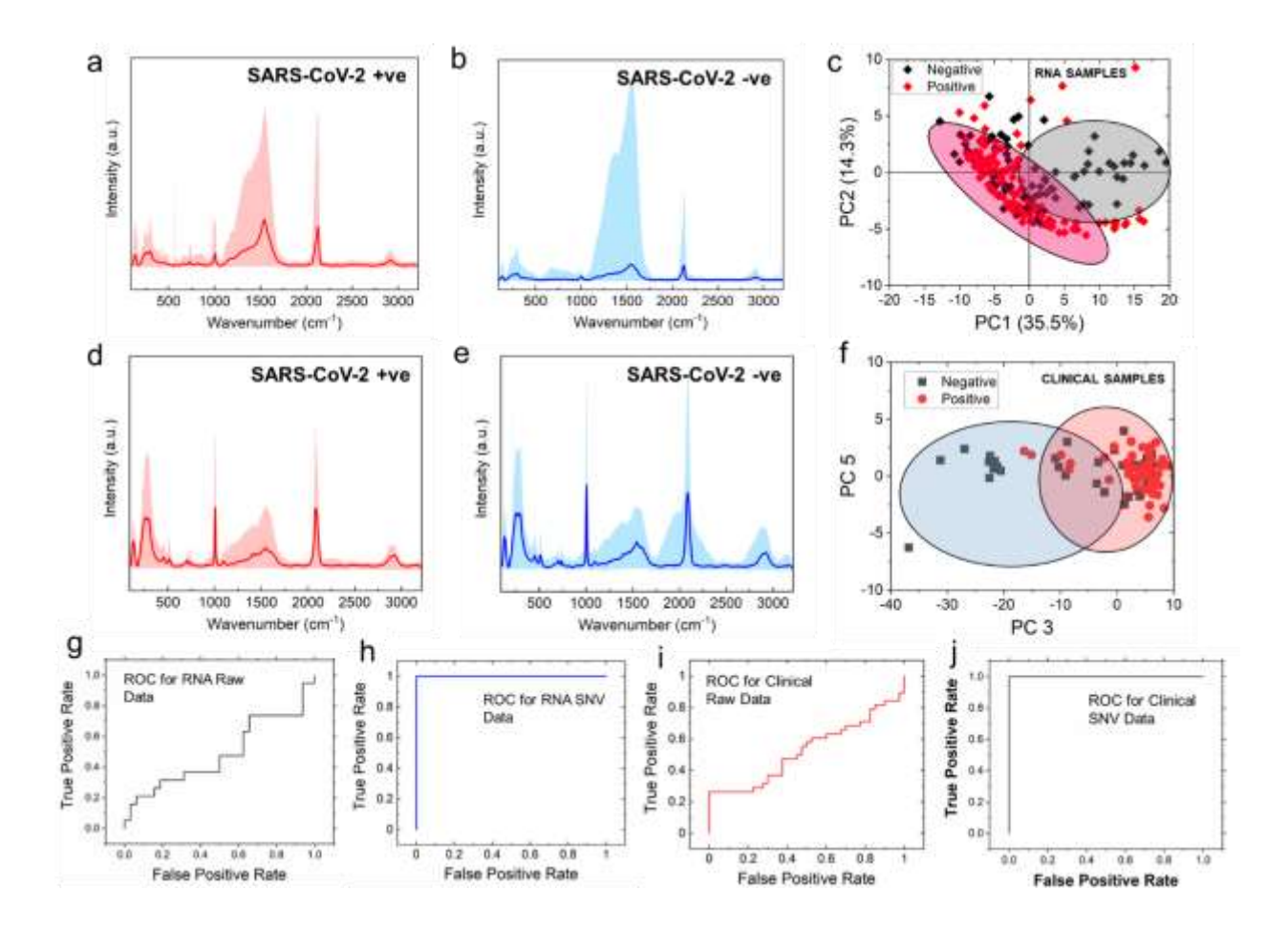


Fig. 4. Representative Raman spectra of N-ASO₁₊₂ capped AuNPs added with RNA extracted from SARS-CoV-2 (a) positive, P1 and (b) negative, N1 clinical samples; The respective representative Raman spectra of N-ASO₁₊₂ capped AuNPs admixed with direct SARS-CoV-2 (d) positive and (e) negative clinical samples are also shown without the extraction of RNA but with just the addition of lysis buffer. The range of all the spectra is shown as shaded color for each sample while the dark color is representing the mean spectra. PCA score plots show the separation between negative and positive samples of

(c) extracted RNA samples and (f) direct clinical samples; ROC curves for (g) raw data and (h) after performing SNV operation on the SERS data obtained with extracted RNA samples; ROC curves for (i) raw data and (j) after performing SNV operation on the SERS data obtained while analyzing the direct clinical samples without any extraction of RNA from N-ASO₁₊₂ capped AuNPs.

2.6. Analyzing the Raman data by machine learning techniques to differentiate among the clinical samples. Here, we realized that only the strong binding affinity among the N-ASO₁₊₂ AuNPs with their target RNA sequences obtained through SERS was not enough in selectively differentiating SARS-CoV-2 positive samples from the negative ones with high confidence value (Carlomagno et al., 2021; Huang et al., 2021; Sanchez et al., 2021; Yin et al., 2021). Hence, we used the Support Vector Machine (SVM) algorithm to improve the predictive performance of our assay. At first, we developed a model based on the training dataset and based on that model we predicted the rest of our dataset. Fig.s 4g and 4i are showing the receiver operating characteristic (ROC) curve of our developed model based on the raw data for RNA and clinical samples respectively. However, when we applied the standard normal variate (SNV) algorithm to perform preprocessing of our dataset followed by training the model, we have observed significant improvement of our model. The performance of the algorithm can be measured based on the specificity and sensitivity of the results as tabulated in **Table S7**. Overall, by applying the SNV operation, we have successfully increased the sensitivity and specificity of the probes for the clinical samples, tested directly without the extraction of RNA, from 30% to ~100% and 50% to 90%, respectively. On the other hand, for isolated RNA

samples, the specificity was increased from 58% to 95% but, the sensitivity did not improve (went from 67% to 65%). The respective ROC curves for the RNA and direct clinical samples fitted after SNV operation are shown in **Fig.s 4h** and **4j** respectively. Thus, we have successfully discriminated SARS-CoV-2 positive and negative samples directly from the clinical nasal swabs with the addition of lysis buffer and N-ASO₁₊₂ AuNPs through a combinatorial effort from SERS and ML-based techniques. Representative Raman microscopic images of N-ASO₁₊₂ capped AuNPs admixed with SARS-CoV-2 positive and negative RNA (**Fig. 5a, b**) and direct clinical samples (**Fig. 5c, d**) has accordingly been acquired. Here, the Raman map for RNA samples had 1500 pixels with 1500 individual Raman spectra, whereas for direct clinical samples, the Raman map had 2500 pixels with 2500 individual Raman spectra.

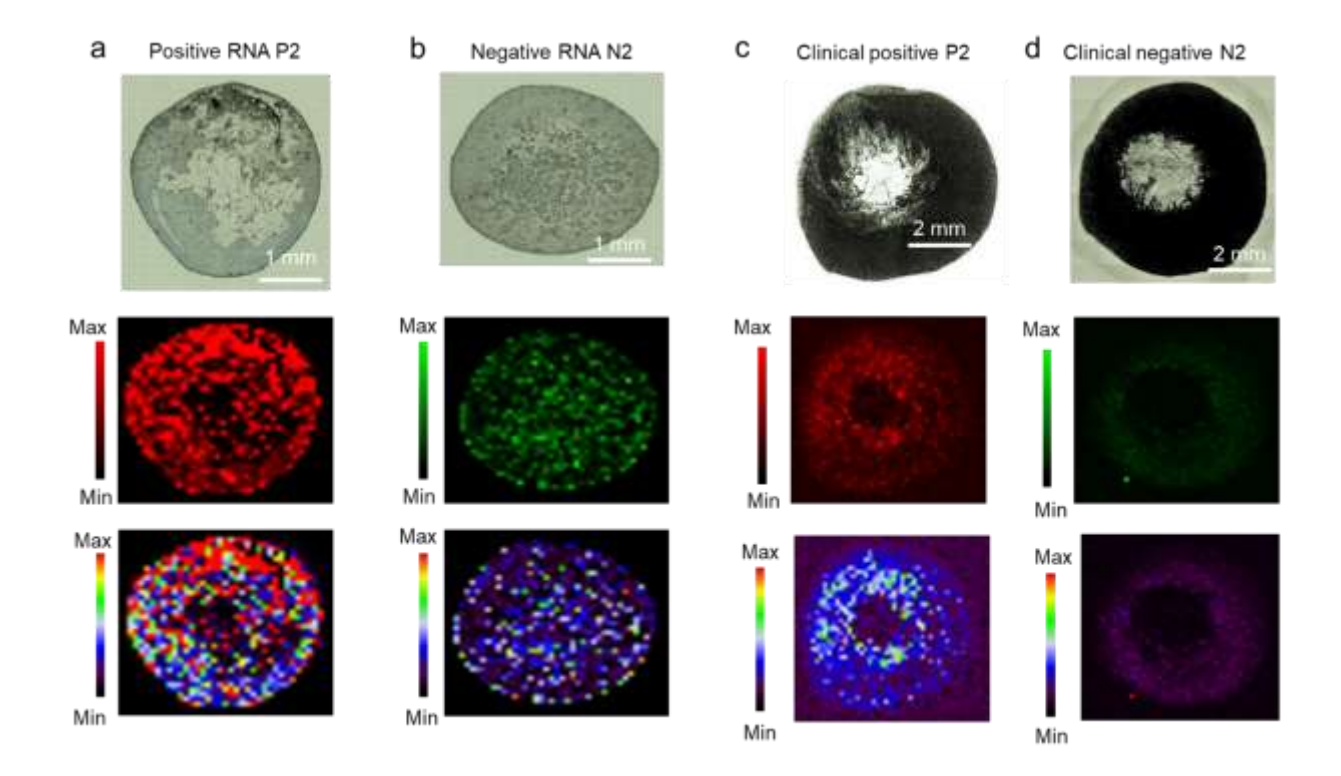


Fig. 5. Representative Raman microscopic images of N-ASO₁₊₂ capped AuNPs admixed with SARS-CoV-2 positive and negative (a, b) extracted RNA and (c, d) direct clinical samples at 928 cm⁻¹ using StreamHR acquisition mode and obtained with 785 nm laser, 100% power, grating of 1200, magnification of 50 XL and exposure time of 0.5 s. The pixel size for RNA and clinical samples were 70μm × 70μm and 200μm × 200μm, respectively. Distribution for whole Raman spectrum is from 200-3200 cm⁻¹. For RNA samples, map has around 1500 pixels (that is 1500 Raman spectra) and for clinical samples, map has around 2500 pixels (that is 2500 Raman spectra).

2.7. Hypothesizing the interaction of developed ASOs with imaginary future N-gene mutations. Thus, we have developed herein a combination of SERS and ML-based methods, which can be utilized to study DNA probes with SARS-CoV-2 wild-type genes

and current mutated forms. Although the present mutations on the SARS-CoV-2 N gene do not hamper the target RNA sites for the developed ASOs, we were interested to see the effect of the mutation at the target RNA site on the binding efficiency of ASOs. Accordingly, we introduced several hypothetical mutations at the target RNA site for N-ASO1 and observed their effect on binding affinity. Considering the fact that single point mutation in a protein sequence will change three consecutive nucleotides, we modified the original target RNA sequence at four different locations with a change in three nucleotides in each case to represent single mutated forms. In a similar way, dual point and triple point mutations were also introduced at the target RNA site. N-ASO1 was then docked with these RNA sequences in HNADOCK server (He et al., 2019), and their respective docking scores were mentioned in Fig. 6a. The docked geometries of N-ASO1 with the original non-mutated target RNA sequence and their mutated forms were shown in Fig. 6. Close monitoring of the ASO-RNA hybridization profiles revealed stable interaction between the two even after a hypothetical single point mutation was introduced at the target RNA site. We observed a drop in docking score and hence in binding affinity when a dual point or triple point mutations were introduced at the target RNA sites.

Target RNA sequences	Docking score with N-ASO1: CCAATGTGATCTTTTGGTGT	(b) 10	(c) 1e
ACACCAAAAGAUCACAUUGG	-862.03	W 80-00	
ACACCAAAAGAUCACAU <mark>ACC</mark>	-823.07	6	100-0-Q
ACACCAAA <mark>CUC</mark> UCACAUUGG	-837.54	9 8	8
ACACCAAAAGA <mark>GGA</mark> CAUUGG	-789.34	8 U 8	
AC <mark>UUC</mark> AAAAGAUCACAUUGG	-805.87	A 626	
AC <mark>UUC</mark> AAAAGA <mark>GGA</mark> CAUUGG	-727.29	10	8
AC <mark>UUC</mark> AAAAGA <mark>GGA</mark> CAU <mark>ACC</mark>	-713.65	20	9
ACACCAAAAGA <mark>GGAGUCACC</mark>	-744.78		9

	ACACCAAAAGAUCACAUUGG ACACCAAAAGAUCACAUACC ACACCAAAACUCUCACAUUGG ACACCAAAAGAGGACAUUGG ACUUCAAAAGAUCACAUUGG ACUUCAAAAGAGGACAUUGG ACUUCAAAAGAGGACAUUGG	ACACCAAAAGAUCACAUUGG -862.03 ACACCAAAAGAUCACAUUGG -823.07 ACACCAAAAGAUCACAUUGG -837.54 ACACCAAAAGAGACAUUGG -789.34 ACUUCAAAAGAUCACAUUGG -805.87 ACUUCAAAAGAUCACAUUGG -727.29 ACUUCAAAAGAGGACAUUGG -713.65	ACACCAAAAGAUCACAUUGG -862.03 ACACCAAAAGAUCACAUACC -823.07 ACACCAAAAGAUCACAUUGG -837.54 ACACCAAAAGAUGACAUUGG -789.34 ACUUCAAAAGAUCACAUUGG -805.87 ACUUCAAAAGAGGACAUUGG -727.29 ACUUCAAAAGAGGACAUUGG -713.65

Fig. 6. (a) List of hypothetical single, double, and triple point mutations on the RNA site targeted by N-ASO1. The hypothetical mutation sites are highlighted with yellow background; (b) Theoretical model of RNA with no mutation; (c) Theoretical model of N-ASO1; Docked model of N-ASO1 with RNA having (d) no mutation sites; (e) single point mutation as shown in no. 4; (f) double point mutations as shown in no. 6; (g) triple point mutations as shown in no. 7 and (h) simultaneous triple point mutations as shown in no. 8.

Thus, this study examined the efficiency of a DNA-based universal probe and its fundamental interaction with the entire known mutated forms of SARS-CoV-2 without any false negative signals through a unique combination of SERS and ML-based approaches. This study also demonstrated that the developed assay will still be effective in case of a future single point mutation at the target site and would only have reduced activity in case of dual or triple point mutations.

3. Conclusions.

Briefly, we have developed herein a unique combination of Surface Enhanced Raman Spectroscopy (SERS) and machine learning (ML) based approaches for studying selective and sensitive interaction with SARS-CoV-2 having any of its current mutations including the recently known Omicron. Several antisense oligonucleotides (ASOs) were developed against N, E and RdRp gene segments of SARS-CoV-2 where N genetargeted ones were found to be most effective. The thiolated N-ASO₁₊₂ capped AuNPs agglomerated in presence of its target RNA sequence and demonstrated a change in its surface plasmon resonance (SPR). The agglomeration of Au-ASO NPs also tuned the size of the generated nanoparticles which was followed by the change in their SERS response. The SERS signal was then evaluated with ML techniques to selectively distinguish among COVID-19 positive and negative samples with high accuracy, sensitivity and specificity. The limit of detection of SARS-CoV-2 RNA was found to be 63 copies/m. The developed quantitative assay was also validated with a range of clinical samples having varying Ct numbers. Thus, this study establishes N gene-targeted ASOs as the critical part of the assay to efficiently detect all the current SARS-CoV-2 variants regardless of their mutations. Further probing into the hybridization profile of the ASOs revealed that the ASO-RNA interaction remained unaltered for any hypothetical single point mutations at the original target RNA site and diminished only in case of the hypothetical double or triple point mutation cases. This approach could therefore have an immediate impact on understanding different mutations associated with SARS-CoV-2, especially during the spread of its current variant, Omicron. To the best of our knowledge, there is no literature report for an effective DNA probe that can selectively hybridize with all the different genomic variants of SARS-CoV-2 with similar sensitivity and specificity without any false negative signals which is one of the most concerning limitations of the current COVID-19 diagnosis.

4. Materials and Methods.

All the chemicals were procured from reputable commercial vendors and used without any further purification steps. The custom designed and thiol-modified ASOs were procured from Sigma Aldrich and stored at -20 °C until further use. All the experiments were carried out at constant room temperature of 25 °C unless otherwise specified.

4.1. Design of antisense oligonucleotides (ASOs). Gene sequences (RdRp: 13,442-16,236; E: 26,245-26,472 and N: 28,274-29,533) from the whole genome sequence of SARS-CoV-2 (wild type isolate SARS-CoV-2/human/USA/WA-CDC-WA1-A12/2020, MT020880) was chosen and multiple ASO sequences of 20 nucleotides in length were selected from Soligo software output (Ding et al., 2004). The choice of ASOs were primarily based on the optimum GC content and theoretically calculated target binding and disruption energies at 37 °C in 1 M NaCl aqueous solution. We propose to select four ASOs, two for the front (ASO1 and ASO2), and two targeting the end region (ASO3 and ASO4) of the gene. The ASOs will also target closely following sequences at each location. Accordingly, four ASOs were selected both for N and E gene, whereas only two were selected for RdRp gene (**Table 1**). We were not able to select more than two ASOs for RdRp gene target as ASOs with high enough binding energies are not available for this target.

- **4.2. Synthesis of gold nanoparticles (AuNPs).** The gold nanoparticles were prepared from a solution of chloroauric acid and sodium citrate following a previously published literature protocol (Kumar et al., 2020; Moitra et al., 2020; Schwartz-Duval et al., 2020). Briefly, 150 mL solution of 2.2 mM sodium citrate was refluxed for 15 min under continuous stirring. 1 mL solution of 25 mM chloroauric acid was then added the boiling solution of sodium citrate. This mixture was kept under reflux for an additional 15 min over which the color of the solution changed from yellow to wine red. The resultant mixture was centrifuged at 25,000 rpm for 10 mins, precipitate collected and washed with milli-Q water for at least two times to remove any reaction contaminations. Finally, the precipitate containing citrate stabilized gold nanoparticles were collected and resuspended in water for future use.
- **4.3. Conjugation of ASOs to AuNPs.** The thiolated ASOs, at a concentration of 1 μ M, were added to a solution of citrate stabilized AuNPs having ~3 × 10¹⁰ particles/mL concentration. The mixture was stirred at room temperature for ~1 hour, centrifuged to remove any excess of uncapped ASO from the supernatant, and the pellet was then resuspended in a similar volume of milli-Q water. The nanoparticles were kept at 4 °C for future use.
- **4.4. UV-Visible absorbance spectroscopy.** The absorbance spectra were acquired on a Biotek Synergy Neo2Microplate Reader.
- **4.5. Dynamic light scattering.** The hydrodynamic diameters of the Au-ASO NPs in presence and absence of their target RNA were monitored on a Malvern Nano S system.

- **4.6. Transmission electron microscopy (TEM).** The N-ASO₁₊₂ AuNPs were investigated under the transmission electron microscope (FEI tecnai T12). The tungsten filament was used as the electron optics, and the voltage was kept constant at 80 kV. A 20 μL sample droplet was spotted onto a carbon-coated copper grid (400 mesh) and allowed to stay there for about 10 min before being removed.
- **4.7. Sample Preparation for Raman analyses.** RNA from the clinical samples were extracted and purified following standard commercial technique. The RNAs were stored in multiple aliquots at -80 °C for future use. This was done to prevent denaturation of the stock RNA samples from excessive freeze thaw.

2 μL of Au-ASO NPs were then mixed with 2 μL of SARS-CoV-2 RNA by gentle pipetting a few times on an ice rack. 2 μL of this mixture were dropped on a clean stainless-steel slide and left to dry at room temperature. Raman spectra of the dried spots were recorded immediately after using a Renishaw inVia Reflex Raman Spectroscope.

For the direct analyses of clinical samples without the extraction of RNA, the samples were added with lysis buffer having guanidine isothiocyanate with a sample: lysis buffer at 2:1 molar ratio. 2 µL of these samples were then added with 2 µL of Au-ASO NPs and mixed properly as discussed earlier for RNA sample before recording Raman spectra.

4.8. Raman Spectroscopy. Raman experiments were performed on the samples with 785 (grating of 1200) and 633 (grating of 1800) nm lasers (laser spot $\sim 1.1 \mu m$; penetration depth \sim a few microns depending on the samples) with 10% of power and 10 s exposure time on mirror-like surface stainless steel slides. High confocality 50 XL long working distance dry objective was used for all the experiments with free working distance

of 8.2 and numerical aperture of 0.5. At least ten spectra were acquired from each sample for statistical analysis in the range of 100-3200 cm⁻¹. Raman images were acquired in StreamHR image acquisition mode by utilizing 785 nm laser (100% power, grating of 1200, 50 XL magnification) with the center of 1200 cm⁻¹ (609-1728 cm⁻¹) by step size (resolution) of 200×200 µm for clinical samples and 70×70 µm for RNA samples. During the Raman imaging, exposure time was set to be 0.5 s. Renishaw WiRE 4.4 was used for date processing and analysis of Raman signals and images. For baseline correction, we used intelligent fitting of WiRE 4.4 with polynomial order of 11 and noise tolerance of 1.5. Subsequent data processing was also performed by OriginLab 2018.

4.9. Statistical Analyses (Principal Component Analysis). After gathering the Raman spectra from the samples, it was corrected by Renishaw's WiRE 4.4 (Windows-based Raman Environment) software. Baseline subtraction was performed for all the data by using intelligent fitting of Wire 4.4 and a polynomial value of 11 was set as default for the fitting. For the further analysis of spectral data we performed Principal Component Analysis (PCA) as we have found it very useful for Raman spectroscopy analysis previously. This multivariate analysis was completed with the "Principal Component Analysis for Spectroscopy" toolbox of Origin Lab 2020 (Origin Lab, Northampton, MA)). The spectral differences were distinguished with Principal components (PC). The PCs were calculated based on the covariance matrix and 8 components were extracted. These parameters were set before performing the analysis and based on the variation of the dataset we received several PCs. Though, mean centering is a common step for calculating principal components, but we didn't have to perform it separately as while computing the covariance matrix the software performed mean centering implicitly. To

visualize the results, we plotted score plot where each point is representing a Raman spectrum separately while selecting two or more PCs. The clustering of each Raman spectra from the score plot shows the separation of the data. Here, we used 95% confidence level to show the clustering of the Raman spectra. In order to find the vibrational fingerprint, we plotted the loading plot calculated from PCA. From the loading plot, we also found the peak locations which dominated the PCA. Besides performing these analyses on raw data, we also used min-max normalization through Origin where the normalization was performed in [0, 1] range. Later, a smoothing operation was also performed to reduce the noise of the dataset with the help of Savitzky-Golay method. During this analysis, window size was selected as 5 and polynomial order was set to 2. Based on these posts processed dataset, PCA was performed in a similar fashion.

4.10. Machine Learning Analysis of Raman Data (SVM Analysis). Besides performing PCA, we also developed an algorithm based on Support vector machine (SVM) analysis. This supervised analysis helps to classify groups. Here based on the Raman spectra we tried to separate our dataset between positive and negative group of samples. Support vector machine classification model by MATLAB was used in our method. Here at first, we trained a model and then predict rest of our dataset Based on the classification results we calculated the specificity and sensitivity of our approach. Later, we used similar approach on a selected range of dataset. Here, the selected range of the wavelength was 400-1800 nm. The reasoning for selecting this range was, we noticed most of the peaks of the dataset located within this range and thus contribution for separation was much higher. Besides this selected range, we performed the Standard Normal Variate (SNV) analysis to improve the results we gathered from previous stage. To get the SNV results

we calculated mean and standard deviation of each of the dataset. The mean value was subtracted from the raw spectra and then it was divided by the standard deviation of that particular dataset. These operations were performed through MATLAB and each dataset was considered as a matrix while performing the calculation.

4.11. Docking analyses. The single stranded models for N-ASO1 and RNA strands (non-mutated and mutated ones) were made in Web 3DNA 2.0 software (Li et al., 2019) and then docked on a HNADOCK server (He et al., 2019) to obtain the docking score and conformationally stable models.

Supporting Information. Figures S1-S7, Tables S1-S7 and materials and methods section have been provided in the supporting information.

Author Contributions

The manuscript was written through the contributions of all authors. All authors have approved the final version of the manuscript.

Notes

The authors declare the following competing financial interest(s): Prof Pan is the founder or co-founder of three university-based start-ups. None of these entities, however, supported this work. All the other authors declare no competing financial interest.

Acknowledgements.

The authors gratefully acknowledge the receipt of funding from the National Institute of Biomedical Imaging and Bioengineering (NIBIB) R03EB028026, R03 EB028026-02S2, and R03 EB028026-02S1, the University of Maryland, Baltimore (UMB), and University of Maryland, Baltimore County (UMBC). MRG is supported by National Science Foundation (NSF CAREER award number: 2045640).

References.

- Abid Hasan, S.M., He, Y., Chang, T.-W., Wang, J., Gartia, M.R., 2019. Detecting DNA Methylation Using Surface-Enhanced Raman Spectroscopy. The Journal of Physical Chemistry C 123, 698–709. https://doi.org/10.1021/acs.jpcc.8b10178
- Alafeef, M., Dighe, K., Moitra, P., Pan, D., 2020. Rapid, Ultrasensitive, and Quantitative Detection of SARS-CoV-2 Using Antisense Oligonucleotides Directed Electrochemical Biosensor Chip. ACS Nano 14, 17028–17045. https://doi.org/10.1021/acsnano.0c06392
- Alafeef, M., Moitra, P., Dighe, K., Pan, D., 2021a. Hyperspectral Mapping for the Detection of SARS-CoV-2 Using Nanomolecular Probes with Yoctomole Sensitivity. ACS Nano 15, 13742–13758. https://doi.org/10.1021/acsnano.1c05226
- Alafeef, M., Moitra, P., Dighe, K., Pan, D., 2021b. RNA-extraction-free nano-amplified colorimetric test for point-of-care clinical diagnosis of COVID-19. Nature Protocols 16, 3141–3162. https://doi.org/10.1038/s41596-021-00546-w
- Barton, M.I., MacGowan, S.A., Kutuzov, M.A., Dushek, O., Barton, G.J., van der Merwe, P.A., 2021. Effects of common mutations in the SARS-CoV-2 Spike RBD and its ligand, the human ACE2 receptor on binding affinity and kinetics. eLife 10, e70658. https://doi.org/10.7554/eLife.70658
- Callaway, E., Ledford, H., 2021. How bad is Omicron? What scientists know so far. Nature 600, 197–199. https://doi.org/10.1038/d41586-021-03614-z
- Carlomagno, C., Bertazioli, D., Gualerzi, A., Picciolini, S., Banfi, P.I., Lax, A., Messina, E., Navarro, J., Bianchi, L., Caronni, A., Marenco, F., Monteleone, S., Arienti, C., Bedoni, M., 2021. COVID-19 salivary Raman fingerprint: innovative approach for the

- detection of current and past SARS-CoV-2 infections. Scientific Reports 11, 4943. https://doi.org/10.1038/s41598-021-84565-3
- Carter, L.J., Garner, L. v., Smoot, J.W., Li, Y., Zhou, Q., Saveson, C.J., Sasso, J.M., Gregg, A.C., Soares, D.J., Beskid, T.R., Jervey, S.R., Liu, C., 2020. Assay Techniques and Test Development for COVID-19 Diagnosis. ACS Central Science 6, 591–605. https://doi.org/10.1021/acscentsci.0c00501
- Chaichi, A., Hasan, S.M.A., Mehta, N., Donnarumma, F., Ebenezer, P., Murray, K.K., Francis, J., Gartia, M.R., 2021. Label-free lipidome study of paraventricular thalamic nucleus (PVT) of rat brain with post-traumatic stress injury by Raman imaging. The Analyst 146, 170–183. https://doi.org/10.1039/D0AN01615B
- Chang, T.-W., Wang, X., Hsiao, A., Xu, Z., Lin, G., Gartia, M.R., Liu, X., Liu, G.L., 2015. Bifunctional Nano Lycurgus Cup Array Plasmonic Sensor for Colorimetric Sensing and Surface-Enhanced Raman Spectroscopy. Advanced Optical Materials 3, 1397–1404. https://doi.org/10.1002/adom.201500092
- Copin, R., Baum, A., Wloga, E., Pascal, K.E., Giordano, S., Fulton, B.O., Zhou, A., Negron, N., Lanza, K., Chan, N., Coppola, A., Chiu, J., Ni, M., Wei, Y., Atwal, G.S., Hernandez, A.R., Saotome, K., Zhou, Y., Franklin, M.C., Hooper, A.T., McCarthy, S., Hamon, S., Hamilton, J.D., Staples, H.M., Alfson, K., Carrion, R., Ali, S., Norton, T., Somersan-Karakaya, S., Sivapalasingam, S., Herman, G.A., Weinreich, D.M., Lipsich, L., Stahl, N., Murphy, A.J., Yancopoulos, G.D., Kyratsous, C.A., 2021. The monoclonal antibody combination REGEN-COV protects against SARS-CoV-2 mutational escape in preclinical and human studies. Cell 184, 3949-3961.e11. https://doi.org/10.1016/j.cell.2021.06.002
- Daria, S., Bhuiyan, M.A., Islam, Md.R., 2021. Detection of highly muted coronavirus variant Omicron (B.1.1.529) is triggering the alarm for South Asian countries: Associated risk factors and preventive actions. Journal of Medical Virology. https://doi.org/10.1002/jmv.27503
- Dighe, K., Moitra, P., Alafeef, M., Gunaseelan, N., Pan, D., 2021. A rapid RNA extraction-free lateral flow assay for molecular point-of-care detection of SARS-CoV-2 augmented by chemical probes. Biosensors and Bioelectronics 113900. https://doi.org/10.1016/j.bios.2021.113900
- Ding, Y., Chan, C.Y., Lawrence, C.E., 2004. Sfold web server for statistical folding and rational design of nucleic acids. Nucleic Acids Research 32, 135–141. https://doi.org/10.1093/nar/gkh449
- Gartia, M.R., Xu, Z., Behymer, E., Nguyen, H., Britten, J.A., Larson, C., Miles, R., Bora, M., Chang, A.S.-P., Bond, T.C., Logan Liu, G., 2010. Rigorous surface enhanced Raman spectral characterization of large-area high-uniformity silver-coated tapered silica nanopillar arrays. Nanotechnology 21, 395701. https://doi.org/10.1088/0957-4484/21/39/395701

- Gitman, M.R., Shaban, M. v., Paniz-Mondolfi, A.E., Sordillo, E.M., 2021. Laboratory Diagnosis of SARS-CoV-2 Pneumonia. Diagnostics 11, 1270. https://doi.org/10.3390/diagnostics11071270
- Harvey, W.T., Carabelli, A.M., Jackson, B., Gupta, R.K., Thomson, E.C., Harrison, E.M., Ludden, C., Reeve, R., Rambaut, A., Peacock, S.J., Robertson, D.L., 2021. SARS-CoV-2 variants, spike mutations and immune escape. Nature Reviews Microbiology 19, 409–424. https://doi.org/10.1038/s41579-021-00573-0
- He, J., Wang, J., Tao, H., Xiao, Y., Huang, S.-Y., 2019. HNADOCK: a nucleic acid docking server for modeling RNA/DNA–RNA/DNA 3D complex structures. Nucleic Acids Research 47, W35–W42. https://doi.org/10.1093/nar/qkz412
- Huang, J., Wen, J., Zhou, M., Ni, S., Le, W., Chen, G., Wei, L., Zeng, Y., Qi, D., Pan, M., Xu, J., Wu, Y., Li, Z., Feng, Y., Zhao, Z., He, Z., Li, B., Zhao, S., Zhang, B., Xue, P., He, S., Fang, K., Zhao, Y., Du, K., 2021. On-Site Detection of SARS-CoV-2 Antigen by Deep Learning-Based Surface-Enhanced Raman Spectroscopy and Its Biochemical Foundations. Analytical Chemistry 93, 9174–9182. https://doi.org/10.1021/acs.analchem.1c01061
- Janik, E., Niemcewicz, M., Podogrocki, M., Majsterek, I., Bijak, M., 2021. The Emerging Concern and Interest SARS-CoV-2 Variants. Pathogens 10, 633. https://doi.org/10.3390/pathogens10060633
- Jungreis, I., Sealfon, R., Kellis, M., 2021. SARS-CoV-2 gene content and COVID-19 mutation impact by comparing 44 Sarbecovirus genomes. Nature Communications 12, 2642. https://doi.org/10.1038/s41467-021-22905-7
- Karim, S.S.A., Karim, Q.A., 2021. Omicron SARS-CoV-2 variant: a new chapter in the COVID-19 pandemic. The Lancet 398, 2126–2128. https://doi.org/10.1016/S0140-6736(21)02758-6
- Kevadiya, B.D., Machhi, J., Herskovitz, J., Oleynikov, M.D., Blomberg, W.R., Bajwa, N., Soni, D., Das, S., Hasan, M., Patel, M., Senan, A.M., Gorantla, S., McMillan, J., Edagwa, B., Eisenberg, R., Gurumurthy, C.B., Reid, S.P.M., Punyadeera, C., Chang, L., Gendelman, H.E., 2021. Diagnostics for SARS-CoV-2 infections. Nature Materials 20, 593–605. https://doi.org/10.1038/s41563-020-00906-z
- Khan, M.S., Misra, S.K., Dighe, K., Wang, Z., Schwartz-Duval, A.S., Sar, D., Pan, D., 2018. Electrically-receptive and thermally-responsive paper-based sensor chip for rapid detection of bacterial cells. Biosensors and Bioelectronics 110, 132–140. https://doi.org/10.1016/j.bios.2018.03.044
- Kumar, K., Moitra, P., Bashir, M., Kondaiah, P., Bhattacharya, S., 2020. Natural tripeptide capped pH-sensitive gold nanoparticles for efficacious doxorubicin delivery both: In vitro and in vivo. Nanoscale 12, 1067–1074. https://doi.org/10.1039/c9nr08475d

- Li, J., Lai, S., Gao, G.F., Shi, W., 2021. The emergence, genomic diversity and global spread of SARS-CoV-2. Nature 600, 408–418. https://doi.org/10.1038/s41586-021-04188-6
- Li, S., Olson, W.K., Lu, X.-J., 2019. Web 3DNA 2.0 for the analysis, visualization, and modeling of 3D nucleic acid structures. Nucleic Acids Research 47, W26–W34. https://doi.org/10.1093/nar/gkz394
- Liu, C., Ginn, H.M., Dejnirattisai, W., Supasa, P., Wang, B., Tuekprakhon, A., Nutalai, R., Zhou, D., Mentzer, A.J., Zhao, Y., Duyvesteyn, H.M.E., López-Camacho, C., Slon-Campos, J., Walter, T.S., Skelly, D., Johnson, S.A., Ritter, T.G., Mason, C., Costa Clemens, S.A., Gomes Naveca, F., Nascimento, V., Nascimento, F., Fernandes da Costa, C., Resende, P.C., Pauvolid-Correa, A., Siqueira, M.M., Dold, C., Temperton, N., Dong, T., Pollard, A.J., Knight, J.C., Crook, D., Lambe, T., Clutterbuck, E., Bibi, S., Flaxman, A., Bittaye, M., Belij-Rammerstorfer, S., Gilbert, S.C., Malik, T., Carroll, M.W., Klenerman, P., Barnes, E., Dunachie, S.J., Baillie, V., Serafin, N., Ditse, Z., da Silva, K., Paterson, N.G., Williams, M.A., Hall, D.R., Madhi, S., Nunes, M.C., Goulder, P., Fry, E.E., Mongkolsapaya, J., Ren, J., Stuart, D.I., Screaton, G.R., 2021. Reduced neutralization of SARS-CoV-2 B.1.617 by vaccine and convalescent serum. Cell 184, 4220-4236.e13. https://doi.org/10.1016/j.cell.2021.06.020
- Mallapaty, S., Callaway, E., Kozlov, M., Ledford, H., Pickrell, J., van Noorden, R., 2021. How COVID vaccines shaped 2021 in eight powerful charts. Nature. https://doi.org/10.1038/d41586-021-03686-x
- Mercatelli, D., Giorgi, F.M., 2020. Geographic and Genomic Distribution of SARS-CoV-2 Mutations. Frontiers in Microbiology 11, 1800. https://doi.org/10.3389/fmicb.2020.01800
- Misra, S.K., Dighe, K., Schwartz-Duval, A.S., Shang, Z., Labriola, L.T., Pan, D., 2018. In situ plasmonic generation in functional ionic-gold-nanogel scaffold for rapid quantitative bio-sensing. Biosensors and Bioelectronics 120, 77–84. https://doi.org/10.1016/j.bios.2018.08.019
- Mohiuddin, M., Kasahara, K., 2022. Investigating the aggressiveness of the COVID-19 Omicron variant and suggestions for possible treatment options. Respiratory Medicine 191, 106716. https://doi.org/10.1016/j.rmed.2021.106716
- Moitra, P., Alafeef, M., Dighe, K., Frieman, M.B., Pan, D., 2020. Selective Naked-Eye Detection of SARS-CoV-2 Mediated by N Gene Targeted Antisense Oligonucleotide Capped Plasmonic Nanoparticles. ACS Nano 14, 7617–7627. https://doi.org/10.1021/acsnano.0c03822
- Moitra, P., Alafeef, M., Dighe, K., Ray, P., Chang, J., Thole, A., Punshon-Smith, B., Tolosa, M., Ramamurthy, S.S., Ge, X., Frey, D.D., Pan, D., Rao, G., 2021a. Rapid and low-cost sampling for detection of airborne SARS-CoV-2 in dehumidifier

- condensate. Biotechnology and Bioengineering 3029–3036. https://doi.org/10.1002/bit.27812
- Moitra, P., Alafeef, M., Dighe, K., Sheffield, Z., Dahal, D., Pan, D., 2021b. Synthesis and characterisation of N-gene targeted NIR-II fluorescent probe for selective localisation of SARS-CoV-2. Chemical Communications 57, 6229–6232. https://doi.org/10.1039/D1CC01410B
- Ostadhossein, F., Sar, D., Tripathi, I., Soares, J., Remsen, E.E., Pan, D., 2020. Oligodots: Structurally Defined Fluorescent Nanoprobes for Multiscale Dual-Color Imaging in Vitro and in Vivo. ACS Applied Materials and Interfaces 12, 10183–10192. https://doi.org/10.1021/acsami.0c00705
- Pachetti, M., Marini, B., Benedetti, F., Giudici, F., Mauro, E., Storici, P., Masciovecchio, C., Angeletti, S., Ciccozzi, M., Gallo, R.C., Zella, D., Ippodrino, R., 2020. Emerging SARS-CoV-2 mutation hot spots include a novel RNA-dependent-RNA polymerase variant. Journal of Translational Medicine 18, 179. https://doi.org/10.1186/s12967-020-02344-6
- Pan, D., Pramanik, M., Senpan, A., Wickline, S.A., Wang, L. v., Lanza, G.M., 2010. A Facile Synthesis of Novel Self-Assembled Gold Nanorods Designed for Near-Infrared Imaging. Journal of Nanoscience and Nanotechnology 10, 8118–8123. https://doi.org/10.1166/jnn.2010.3034
- Pan, D., Pramanik, M., Wickline, S.A., Wang, L. v., Lanza, G.M., 2011. Recent advances in colloidal gold nanobeacons for molecular photoacoustic imaging. Contrast Media and Molecular Imaging 6, 378–388. https://doi.org/10.1002/cmmi.449
- Petrova, V.N., Russell, C.A., 2018. The evolution of seasonal influenza viruses. Nature Reviews Microbiology 16, 47–60. https://doi.org/10.1038/nrmicro.2017.118
- Prasad, A., Chaichi, A., Mahigir, A., Sahu, S.P., Ganta, D., Veronis, G., Gartia, M.R., 2020. Ripple mediated surface enhanced Raman spectroscopy on graphene. Carbon 157, 525–536. https://doi.org/10.1016/j.carbon.2019.09.078
- Rump, L. v, Asamoah, B., Gonzalez-Escalona, N., 2010. Comparison of commercial RNA extraction kits for preparation of DNA-free total RNA from Salmonella cells. BMC Research Notes 3, 211. https://doi.org/10.1186/1756-0500-3-211
- Sanchez, J.E., Jaramillo, S.A., Settles, E., Velazquez Salazar, J.J., Lehr, A., Gonzalez, J., Rodríguez Aranda, C., Navarro-Contreras, H.R., Raniere, M.O., Harvey, M., Wagner, D.M., Koppisch, A., Kellar, R., Keim, P., Jose Yacaman, M., 2021. Detection of SARS-CoV-2 and its S and N proteins using surface enhanced Raman spectroscopy. RSC Advances 11, 25788–25794. https://doi.org/10.1039/D1RA03481B
- Schwartz-Duval, A.S., Konopka, C.J., Moitra, P., Daza, E.A., Srivastava, I., Johnson, E. v., Kampert, T.L., Fayn, S., Haran, A., Dobrucki, L.W., Pan, D., 2020. Intratumoral

- generation of photothermal gold nanoparticles through a vectorized biomineralization of ionic gold. Nature Communications 11, 4530. https://doi.org/10.1038/s41467-020-17595-6
- Shrivastav, A.M., Cvelbar, U., Abdulhalim, I., 2021. A comprehensive review on plasmonic-based biosensors used in viral diagnostics. Communications Biology 4, 70. https://doi.org/10.1038/s42003-020-01615-8
- Srivastava, I., Misra, S.K., Bangru, S., Boateng, K.A., Soares, J.A.N.T., Schwartz-Duval, A.S., Kalsotra, A., Pan, D., 2020. Complementary Oligonucleotide Conjugated Multicolor Carbon Dots for Intracellular Recognition of Biological Events. ACS Applied Materials and Interfaces 12, 16137–16149. https://doi.org/10.1021/acsami.0c02463
- Telenti, A., Arvin, A., Corey, L., Corti, D., Diamond, M.S., García-Sastre, A., Garry, R.F., Holmes, E.C., Pang, P.S., Virgin, H.W., 2021. After the pandemic: perspectives on the future trajectory of COVID-19. Nature 596, 495–504. https://doi.org/10.1038/s41586-021-03792-w
- Wang, L., Zhou, T., Zhang, Y., Yang, E.S., Schramm, C.A., Shi, W., Pegu, A., Oloniniyi, O.K., Henry, A.R., Darko, S., Narpala, S.R., Hatcher, C., Martinez, D.R., Tsybovsky, Y., Phung, E., Abiona, O.M., Antia, A., Cale, E.M., Chang, L.A., Choe, M., Corbett, K.S., Davis, R.L., DiPiazza, A.T., Gordon, I.J., Hait, S.H., Hermanus, T., Kgagudi, P., Laboune, F., Leung, K., Liu, T., Mason, R.D., Nazzari, A.F., Novik, L., O'Connell, S., O'Dell, S., Olia, A.S., Schmidt, S.D., Stephens, T., Stringham, C.D., Talana, C.A., Teng, I.-T., Wagner, D.A., Widge, A.T., Zhang, B., Roederer, M., Ledgerwood, J.E., Ruckwardt, T.J., Gaudinski, M.R., Moore, P.L., Doria-Rose, N.A., Baric, R.S., Graham, B.S., McDermott, A.B., Douek, D.C., Kwong, P.D., Mascola, J.R., Sullivan, N.J., Misasi, J., 2021. Ultrapotent antibodies against diverse and highly transmissible SARS-CoV-2 variants. Science 373, 759. https://doi.org/10.1126/science.abh1766
- Wang, P., Nair, M.S., Liu, L., Iketani, S., Luo, Y., Guo, Y., Wang, M., Yu, J., Zhang, B., Kwong, P.D., Graham, B.S., Mascola, J.R., Chang, J.Y., Yin, M.T., Sobieszczyk, M., Kyratsous, C.A., Shapiro, L., Sheng, Z., Huang, Y., Ho, D.D., 2021. Antibody resistance of SARS-CoV-2 variants B.1.351 and B.1.1.7. Nature 593, 130–135. https://doi.org/10.1038/s41586-021-03398-2
- Wozniak, A., Cerda, A., Ibarra-Henríquez, C., Sebastian, V., Armijo, G., Lamig, L., Miranda, C., Lagos, M., Solari, S., Guzmán, A.M., Quiroga, T., Hitschfeld, S., Riveras, E., Ferrés, M., Gutiérrez, R.A., García, P., 2020. A simple RNA preparation method for SARS-CoV-2 detection by RT-qPCR. Scientific Reports 10, 16608. https://doi.org/10.1038/s41598-020-73616-w
- Xu, Z., Gartia, M.R., Choi, C.J., Jiang, J., Chen, Y., Cunningham, B.T., Liu, G.L., 2011. Quick detection of contaminants leaching from polypropylene centrifuge tubes with

- surface-enhanced Raman spectroscopy and ultraviolet absorption spectroscopy. Journal of Raman Spectroscopy 42, 1939–1944. https://doi.org/10.1002/jrs.2950
- Xu, Z., Jiang, J., Gartia, M.R., Liu, G.L., 2012. Monolithic Integrations of Slanted Silicon Nanostructures on 3D Microstructures and Their Application to Surface-Enhanced Raman Spectroscopy. The Journal of Physical Chemistry C 116, 24161–24170. https://doi.org/10.1021/jp308162c
- Yin, G., Li, L., Lu, S., Yin, Y., Su, Y., Zeng, Y., Luo, M., Ma, M., Zhou, H., Orlandini, L., Yao, D., Liu, G., Lang, J., 2021. An efficient primary screening of COVID-19 by serum Raman spectroscopy. Journal of Raman Spectroscopy 52, 949–958. https://doi.org/10.1002/jrs.6080
- Yu, C.Y., Chan, K.G., Yean, C.Y., Ang, G.Y., 2021. Nucleic Acid-Based Diagnostic Tests for the Detection SARS-CoV-2: An Update. Diagnostics 11, 53. https://doi.org/10.3390/diagnostics11010053
- Zhu, X., Wang, X., Li, S., Luo, W., Zhang, X., Wang, C., Chen, Q., Yu, S., Tai, J., Wang, Y., 2021. Rapid, Ultrasensitive, and Highly Specific Diagnosis of COVID-19 by CRISPR-Based Detection. ACS Sensors 6, 881–888. https://doi.org/10.1021/acssensors.0c01984